NANO LETTERS
Letter
Cite This: Nano Lett. 2018, 18, 6778−6788
pubs.acs.org/NanoLett

# Dual-Stimuli Responsive Bismuth Nanoraspberries for Multimodal Imaging and Combined Cancer Therapy

Zhenglin Li,[†,‡,§] Ying Hu,[£] Zhaohua Miao,[¥] Han Xu,[∥] Chunxiao Li,[∥] Yan Zhao,[‡] Zhuo Li,[†] Manli Chang,[∫] Zhuo Ma,[£] Ye Sun,[*,‡] Flemming Besenbacher,[*,§] Peng Huang,[*,∥] and Miao Yu[*,†]

[†]State Key Laboratory of Urban Water Resource and Environment, School of Chemistry and Chemical Engineering, Harbin Institute of Technology, Harbin 150001, China

[∥]Guangdong Key Laboratory for Biomedical Measurements and Ultrasound Imaging, Laboratory of Evolutionary Theranostics, School of Biomedical Engineering, Health Science Center, Shenzhen University, Shenzhen 518060, China

[‡]Condensed Matter Science and Technology Institute, Harbin Institute of Technology, Harbin 150001, China

[§]Interdisciplinary Nanoscience Center (iNANO) and Department of Physics and Astronomy, Aarhus University, Aarhus 8000, Denmark

[£]School of Life Science and Technology, Harbin Institute of Technology, Harbin 150001, China

[¥]School of Materials Science and Engineering, Harbin Institute of Technology, Harbin 150001, China

[∫]Department of Laboratory Medicine, The Second Affiliated Hospital of Harbin Medical University, Harbin 150001, China

Supporting Information

**ABSTRACT:** Development of stimuli-responsive theranostics is of great importance for precise cancer diagnosis and treatment. Herein, bovine serum albumin (BSA) modified bismuth nanoraspberries (Bi-BSA NRs) are developed as cancer theranostic agents for multimodal imaging and chemo-photothermal combination therapy. The Bi-BSA NRs are synthesized in aqueous phase via a facile reduction method using $Bi_2O_3$ nanospheres as the sacrificial template. The morphology, biocompatibility, photothermal effect, drug loading/releasing abilities, chemotherapy effect, synergistic chemo-photothermal therapy efficacy, and multimodal imaging capacities of Bi-BSA NRs have been investigated. The results show that the NRs possess multiple unique features including (i) raspberry-like morphology with high specific surface area (~52.24 $m^2 \cdot g^{-1}$) and large cavity (total pore volume ~0.30 $cm^3 \cdot g^{-1}$), promising high drug loading capacity (~69 wt %); (ii) dual-stimuli responsive drug release, triggered by acidic pH and NIR laser irradiation; (iii) infrared thermal (IRT), photoacoustic (PA) and X-ray computed tomography (CT) trimodality imaging with the CT contrast enhanced efficiency as high as ~66.7 HU·mL·$mg^{-1}$; (iv) 100% tumor elimination through the combination chemo-photothermal therapy. Our work highlights the great potentials of Bi-BSA NRs as a versatile theranostics for multimodal imaging and combination therapy.

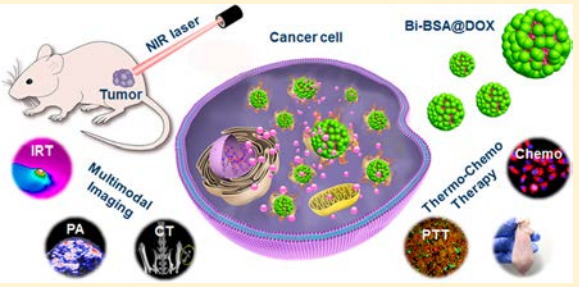


**KEYWORDS:** *Bismuth nanoraspberry, multimodal imaging, drug delivery, chemo-photothermal therapy, theranostics*

Nanoparticle-based drug delivery systems (NDDSs) hold a great promise for overcoming inherent defects of traditional chemotherapy.[1−3] Particularly, stimuli-responsive NDDSs which are sensitive to external physical stimuli (light, magnetic field, etc.) or tumor microenvironment (acidic pH, $H_2O_2$, hypoxia, etc.) are highly desired to realize controllable drug release at targeted sites and to avoid premature drug leakage in normal tissues.[4−7] So far, numerous nanomaterials such as mesoporous silica,[8] liposomes,[9] polymeric micelles,[10] and magnetic nanoparticles[11] have been developed as promising NDDSs for cancer treatment. However, these NDDSs have limitations including relatively low drug loading capacity and the possible drug leakage during their biological circulation, which impeded their further wide applications. Moreover, stand-alone chemotherapy frequently failed to completely eliminate tumor tissues due to the limited therapeutic efficiency and multiple drug resistance of cancer cells,[12] resulting in tumor regeneration or metastasis. Therefore, there is a high demand on multistimuli-responsive NDDSs for precise cancer diagnosis and treatment.

Fortunately, photothermal therapy (PTT) has quickly emerged as a potent complementary approach to enhance chemotherapeutic efficiency.[13−15] PTT employs photothermal conversion agents (PTCAs) to convert photoenergy in the near-infrared (NIR) range into heat, and specifically destroy tumor tissues by this means.[16−18] Since sensitive imaging

Received: June 28, 2018
Revised: September 29, 2018
Published: October 5, 2018






DOI: 10.1021/acs.nanolett.8b02639
Nano Lett. 2018, 18, 6778−6788

**Scheme 1. Schematic Illustration of the Design and Bioapplications of the Bi-BSA NRs**

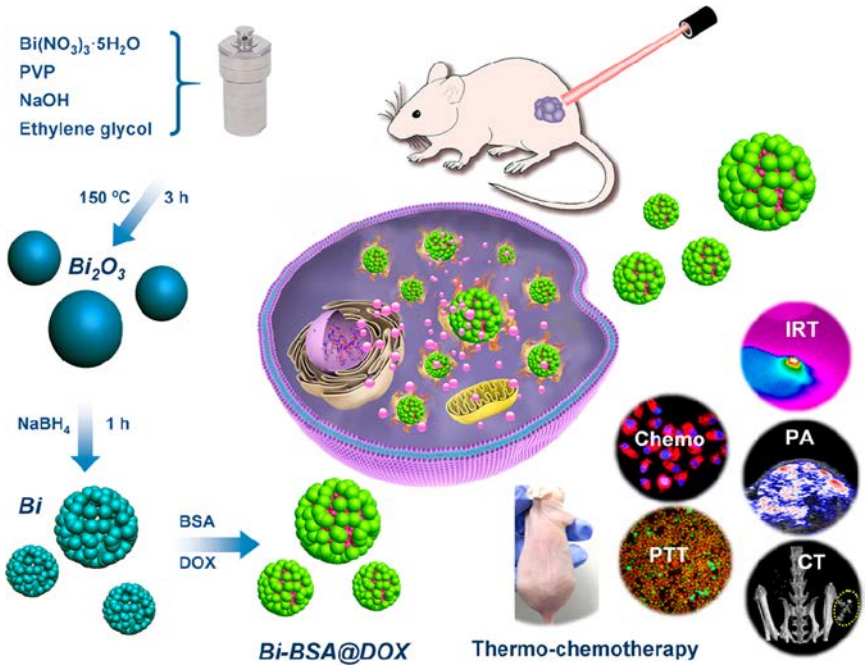


capability of nanomaterials holds great potentials for accurate disease diagnosis, real-time guiding/monitoring therapeutic process,[19,20] and visualization of various cellular behaviors/response,[21−24] it is quite fascinating to integrating imaging functions into PTCAs for a precise, controllable and visualized PTT treatment. So far, various PTCAs have been reported for PTT, including gold nanostructures, carbon-based nanomaterials, transition metal chalcogenides, polymer nanoparticles, and so on.[25−28] Recently, Bi-based PTCAs ($Bi_2Se_3$, $Bi_2S_3$) have sparked extensive interests due to their distinct advantages, including prominent biocompatibility and metabolizability in vivo, low-cost and facile synthesis, high photothermal conversion efficiency and photostability, as well as accessional high-contrast X-ray computed topography (CT) imaging capability.[29−35] Inspiringly, pure metallic Bi nanoparticles have been newly explored as a promising PTCA for efficient photothermal ablation of tumors, showing much superiority over other PTCAs.[36−38] Unfortunately, insufficient tumor eradication and partial tumor recurrence could be observed in these recent reports, possibly due to the intrinsic shortcomings of PTT, such as inevitable depth-dependent attenuation of laser intensity and discrepant heat distribution in tumor tissues.[39] Therefore, it is urgent to endow drug-delivery function for the Bi PTCAs for synergistic chemo-photothermal therapy (CPTT), which remains unexplored up to now. Directing at this aim, two common and straightforward strategies would be (1) encapsulating the Bi PTCAs in porous shells (e.g., mesoporous silica); (2) modifying it with certain polymers that can absorb drug molecules on the PTCAs' surface. However, these strategies suffer from multiple synthesis procedures, elaborated compositions, or poor drug loading capacity.[35,40,41] More seriously, the photothermal conversion performance and CT imaging ability could be severely compromised due to the decreased Bi PTCA proportion after shell coating. An alternative strategy is to synthesize two-dimensional (2D) ultrathin-nanosheet or highly porous nanostructured Bi PTCAs, which inherently possess high specific surface area (SSA). An inherent high-SSA PTCA can already be a favorable cargo for drug delivery with high drug loading capacity. Therefore, the fabrication of high-SSA Bi PTCAs could be very fascinating and promising to realize the high drug loading for synergistic CPTT.

Herein, we report the synthesis of bovine serum albumin (BSA) modified bismuth nanoraspberries (Bi-BSA NRs) as theranostic agents for multimodal imaging and synergistic CPTT (Scheme 1). Utilizing $Bi_2O_3$ nanospheres (NSs) as the sacrificial template, the NRs are synthesized straightforwardly in aqueous phase by a facile reduction method, followed by BSA modification to enhance the dispersibility and stability. The resultant NRs possess a distinct porous nanostructure (SSA ∼ 52.24 $m^2 \cdot g^{-1}$), resulting in a drug loading capacity as high as ∼69 wt %. The NRs exhibit a controllable drug release manner triggered by both laser irradiation and acidic pH. Moreover, benefiting from the strong NIR absorption and high photothermal conversion efficiency of ∼27.1%, a pronounced photothermal effect is demonstrated. By integrating PTT and chemotherapy, the DOX-loaded NRs can realize 100% tumor elimination on mice through the synergistic chemo-photothermal therapy. In addition, due to the high photothermal conversion ability and X-ray attenuation coefficient, the Bi-BSA NRs show great potentials as multimodal contrast agents for infrared thermal (IRT), photoacoustic (PA), and CT triple-modal imaging. This work develops a stimuli-responsive drug-delivery theranostic nanoplatform based on a single-component metallic Bi PTCA for multimodal imaging and synergistic CPTT of tumor.

Utilizing $Bi_2O_3$ NSs as the Bi precursor and template, we for the first time report the formation of raspberry-like Bi nanoparticles with distinct porous structure via a facile reduction method (Scheme 1). The precursor $Bi_2O_3$ NSs were synthesized through a one-pot solvothermal method, in which bismuth nitrate pentahydrate was used as the Bi source, polyvinylpyrrolidone (PVP) as the stabilizing agent, and ethylene glycol (EG) as the reaction solvent. Typical scanning



DOI: 10.1021/acs.nanolett.8b02639
Nano Lett. 2018, 18, 6778−6788

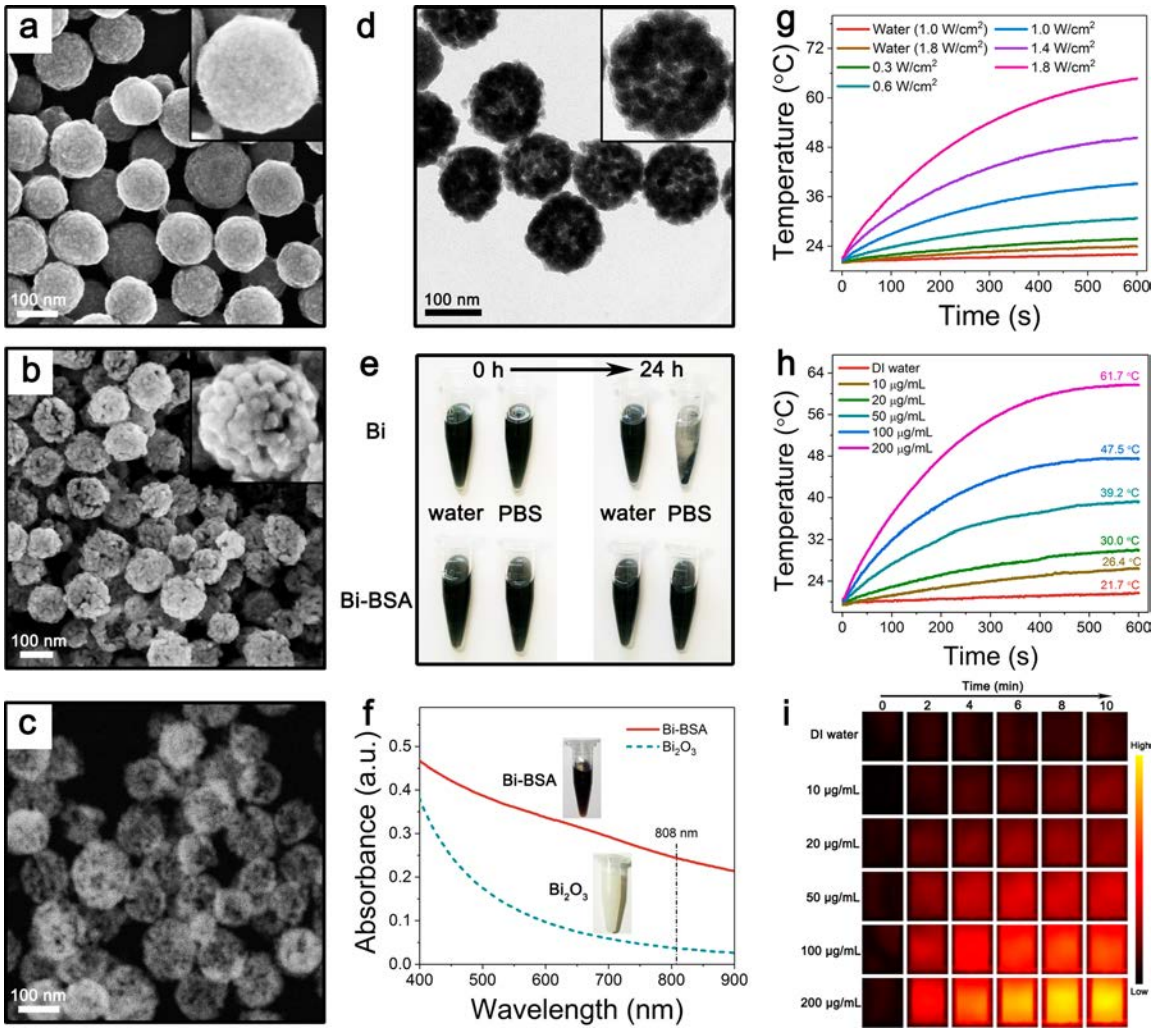


**Figure 1.** Representative SEM images of (a) the $Bi_2O_3$ NSs and (b) the Bi NRs. (c) Typical backscattered electron SEM image and (d) TEM image of the Bi NRs. (e) Digital photos of the Bi and Bi-BSA NRs in water and PBS. (f) UV−Vis−NIR absorption spectra of the $Bi_2O_3$ NSs and Bi-BSA NRs. (g) Photothermal heating curves of pure DI water and the Bi-BSA NRs dispersions (50 $\mu g \cdot mL^{-1}$) upon laser irradiation at gradient power densities. (h) Photothermal heating curves and (i) IRT images of the NRs dispersions at various concentrations under irradiation (1.0 $W \cdot cm^{-2}$).

electron microscopy (SEM) and transmission electron microscopy (TEM) images reveal that the $Bi_2O_3$ NSs were spherical nanoparticles with relatively smooth surfaces (Figure 1a and S1a). On the basis of the statistical result from the TEM images, the average size of the $Bi_2O_3$ NSs was ∼120 nm (Figure S1b). Besides, the energy dispersive spectroscopy (EDS) analysis confirms the intense Bi element signals in the $Bi_2O_3$ NSs sample (Figure S2).

To obtain the highly porous Bi NRs, the $Bi_2O_3$ NSs were used as the sacrificial templates, and the reduction was triggered by dropwise addition of sodium borohydride ($NaBH_4$) aqueous solution under vigorous stirring. Upon the addition, $NaBH_4$ continuously reduced $Bi_2O_3$ to metallic Bi immediately meanwhile entered the porous channels, generating larger pores in the resultant nanostructures. This synthesis method in aqueous phase is simple and rapid and can render the Bi NRs high hydrophilia. Representative SEM image of the resultant Bi NRs reveals their distinct spherical raspberry-shape nanostructure with three-dimensional (3D) cavities stacked by small Bi dots (Figure 1b). The backscattered electron SEM image (Figure 1c) clearly shows their plentiful cavities. The SSA, pore volume, and distribution were then investigated via Brunauer−Emmett−Teller (BET) method. The result in Figure S3a presents a typical type-IV $N_2$ adsorption−desorption isotherm with hysteresis loops, indicating the typical porous nanostructure (Figure S3b). The SSA and total pore volume were measured to be ∼52.24 $m^2 \cdot g^{-1}$ and ∼0.30 $cm^3 \cdot g^{-1}$, respectively. Except the C signals (attributed to the carbon substrate for sample measurement), only intense Bi signal peaks were detected in the EDS spectrum (Figure S4). Powder X-ray diffraction (XRD) pattern (Figure S5) shows that all the diffraction peaks are well indexed to hexagonal Bi (PDF#85-1329), suggesting the high purity. Typical TEM image of the Bi NRs is shown in Figure 1d, where the contrast variation of the individual NRs also confirms their raspberry-like morphology and highly porous nature. The average size of the NRs were ∼123 nm (Figure S6), consistent with that of the $Bi_2O_3$ NSs templates (∼120 nm). The Bi NRs could be well dispersed in DI water with an average hydrodynamic size of ∼127 nm (Figure S7).

However, the as-prepared NRs would easily aggregate in the presence of salts (Figure 1e) due to the electron screening



DOI: 10.1021/acs.nanolett.8b02639
Nano Lett. 2018, 18, 6778−6788

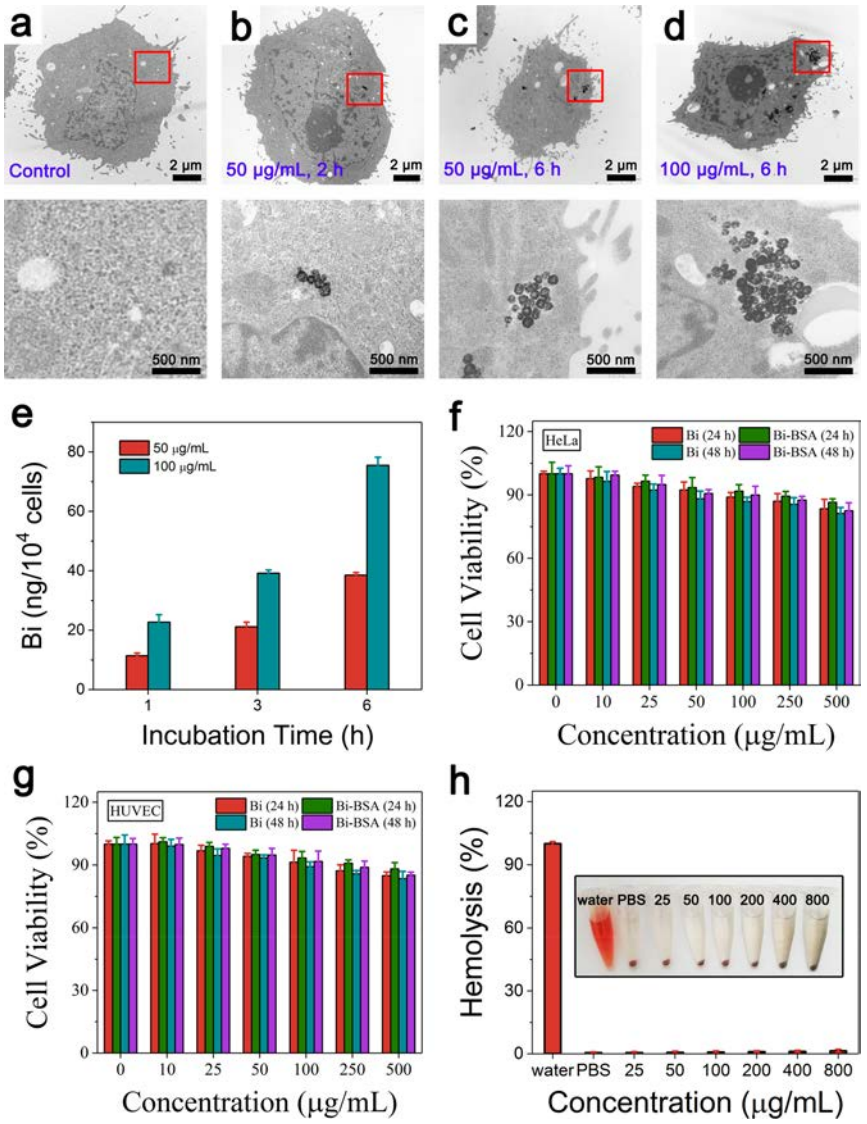


**Figure 2.** (a–d) Typical TEM images of HeLa cells before (Control) or after incubated with the Bi-BSA NRs. The lower-row images are the corresponding zoom-in sections marked by the red squares. (e) Quantitative cellular uptake study analyzed by inductively coupled plasma mass spectrometry (ICP-MS) measurement. Cell viability of (f) HeLa and (g) HUVEC cells after incubation with the bare Bi NRs or Bi-BSA NRs for 24 and 48 h. (h) Hemolysis test of the NRs on RBCs.

effect. BSA, a natural protein (commercially available) with excellent biocompatibility and colloidal stability, was chosen to modify the Bi NRs. BSA can anchor onto inorganic nanoparticles through physical adsorption[42,43] and preferentially bind with metal ions due to the abundant active groups such as N-terminal amine, carboxyl groups in aspartic residues, and thiol groups in cysteine.[44−46] In addition, the abundant functional groups of BSA offer the NRs great convenience of further functionalization with specific-binding molecules (like folic acid, antibodies) to realize active targeting of tumors hence prevent nonspecific uptake of the NRs on normal tissues.[44,46,47] After modification, the obtained Bi-BSA NRs showed remarkably enhanced dispersibility and stability, without any detectable agglomeration in water, phosphate-buffered saline (PBS), cell medium and serum over time (Figure 1e, Figure S8, Figure S9−S11). Three well-resolved characteristic peaks of BSA appeared in the Fourier transform-infrared (FT-IR) spectrum of the Bi-BSA NRs (Figure S12), indicating the successful BSA modification. Moreover, the average hydrodynamic size of the Bi-BSA NRs was measured to be ∼134 nm (Figure S13), a little larger than that of the bare Bi NRs (∼127 nm) (Figure S7). Meanwhile, the Bi-BSA NRs were strongly negative-charged (−29.78 ± 1.55 mV), much higher than that of the pristine Bi NRs (− 9.88 ± 1.19 mV) (Figure S14). Importantly, the Bi-BSA NRs aqueous dispersion (transparent black color) showed a strong broad-band absorption from 400 to 900 nm (Figure 1f), which is in sharp contrast to the $Bi_2O_3$ sample (milk white color). In addition, the NIR optical absorbance of the NRs is highly associated with their concentrations, as evidenced by the perfect linearly incremental 808 nm absorbance with the increased concentrations in both water and cell medium (Figure S15 and S16). Such high NIR absorbance can significantly benefit their photothermal effect.

Next, we studied the photothermal performance by irradiating the Bi-BSA NRs aqueous dispersions (0−200 $\mu g \cdot mL^{-1}$) with a NIR laser (808 nm, 0.3−1.8 $W \cdot cm^{-2}$). Choosing 808 nm laser for PTT application is based on its minimal



DOI: 10.1021/acs.nanolett.8b02639
Nano Lett. 2018, 18, 6778−6788

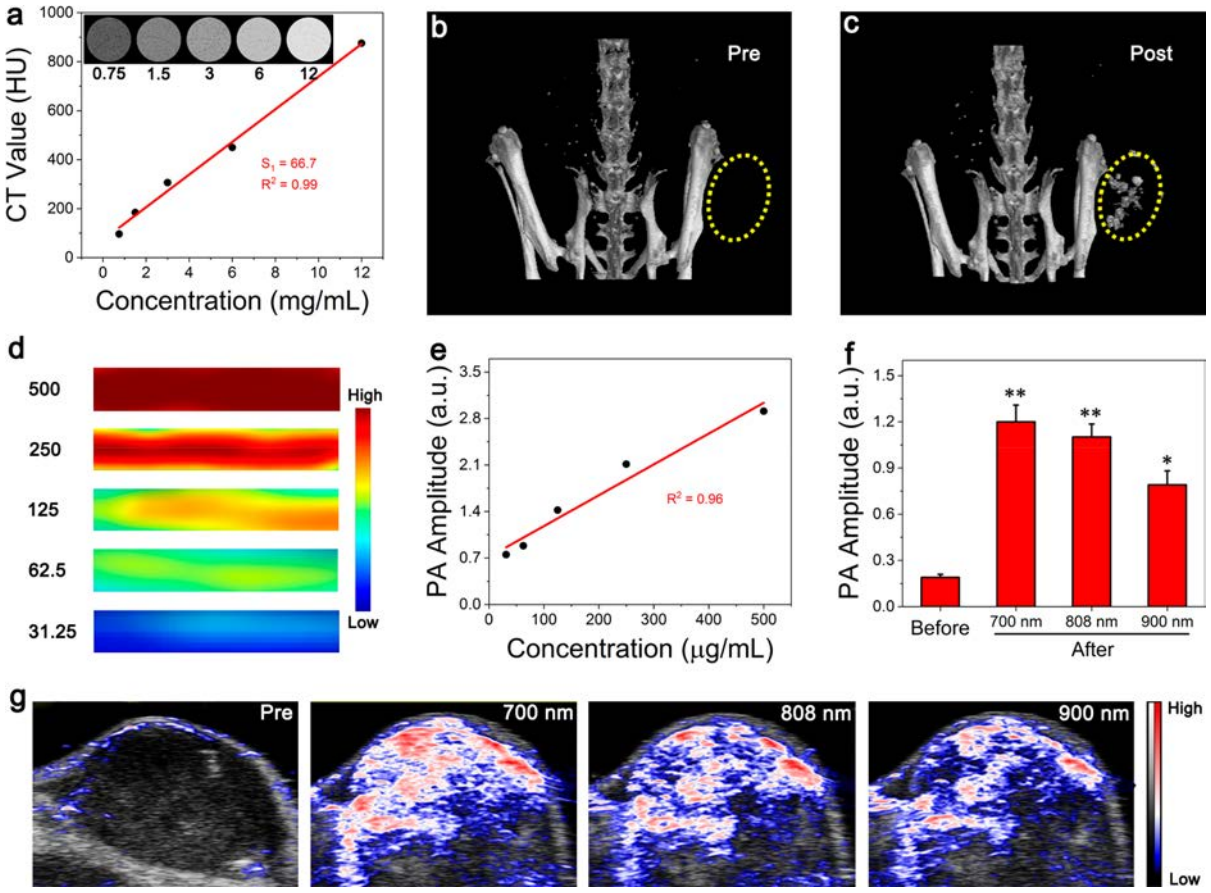


**Figure 3.** CT and PA imaging. (a) CT images and values of the Bi-BSA NRs dispersions at various concentrations (unit: mg·mL$^{-1}$). The 3D in vivo CT images of HeLa tumor-bearing mice (b) before (Pre) and (c) after the NRs injection. The tumor area is marked by the yellow circle. (d) PA images and (e) PA amplitudes of the NRs dispersions at various concentrations (unit: $\mu$g·mL$^{-1}$) upon 808 nm laser irradiation. (f) PA signal intensity and (g) PA images of HeLa tumors on mice before (Pre) and after injection with the NRs employing different NIR wavelengths (700, 808, and 900 nm). Student's $t$ test, *$p$ < 0.05, **$p$ < 0.01.

absorption coefficient (<0.05 cm$^{-1}$) and deep penetration (up to several centimeters depending on the laser power and the tissue type) in biological tissues.[48] Interestingly, the temperature of the NRs dispersions could be dramatically elevated upon the irradiation (ambient temperature of the systems: 19−21 °C), and such photothermal effect highly depended on the applied laser power density, irradiation duration, and NRs concentration (Figure 1g,h). For 50 $\mu$g·mL$^{-1}$ NRs dispersion upon 10 min irradiation at gradient laser power densities (0.3, 0.6, 1.0, 1.4, 1.8 W·cm$^{-2}$), the system temperature reached ∼25.8, 30.8, 39.2, 50.3, and 64.7 °C, respectively (Figure 1g). On the other hand, when the NRs concentrations were gradually increased from 10 to 200 $\mu$g·mL$^{-1}$, the temperature elevation ($\Delta T$) was ∼7.0, 9.8, 18.9, 27.4, and 41.1 °C, respectively (Figure 1h and Figure S17). In marked contrast, pure deionized (DI) water only showed negligible temperature increase (∼1.9 °C for 1.0 W·cm$^{-2}$, ∼3.9 °C for 1.8 W·cm$^{-2}$) under identical conditions. Importantly, the strong photothermal effect also provided excellent signal contrast for IRT imaging, and the intensity was also strongly dependent on the laser power density, irradiation duration and sample concentration (Figure 1i and Figure S18). Using the calculation method reported by Roper et al.,[49] the photothermal conversion efficiency of the NRs was calculated to be ∼27.1% (Figure S19a,b), which is higher than that of the widely studied Au nanorods (21%) and Au nanoshells (13%).[50]

Prior to assessing the biocompatibility, we first studied the cellular uptake efficacy of the Bi-BSA NRs. Different from HeLa cells in the control group (Figure 2a), the Bi-BSA NRs can be visualized in cytoplasmic vesicles mainly via nonspecific cell endocytosis[51,52] after incubation, and the internalized NRs amount increased commensurately with the incubation time and concentration (Figure 2b−d). This phenomenon was further confirmed by the quantitative cellular uptake study (Figure 2e), that is, the cellular uptake efficacy steadily followed incubation time- and concentration-dependent manners. These results reveal the efficient cellular uptake of the NRs by cancer cells.[53] We then performed Cell Counting Kit-8 (CCK-8) assay to examine cytotoxicity of the bare Bi NRs and the Bi-BSA NRs. The cell viability of neither HeLa cells nor human umbilical vein endothelial cells (HUVEC) was affected after incubated with the Bi NRs or Bi-BSA NRs for 24 or 48 h (Figure 2f,g), suggesting no appreciable cytotoxicity at the tested concentrations. It is noticed that at a given concentration the cell viability after incubated with the Bi-BSA NRs is even slightly higher than the Bi NRs-treated case, suggesting that BSA modification can further improve the biocompatibility. Moreover, hemolysis (Figure 2h) and hemagglutination (Figure S20) assays revealed no adverse impact of the Bi-BSA NRs on red blood cells (RBCs). All these



DOI: 10.1021/acs.nanolett.8b02639
Nano Lett. 2018, 18, 6778−6788

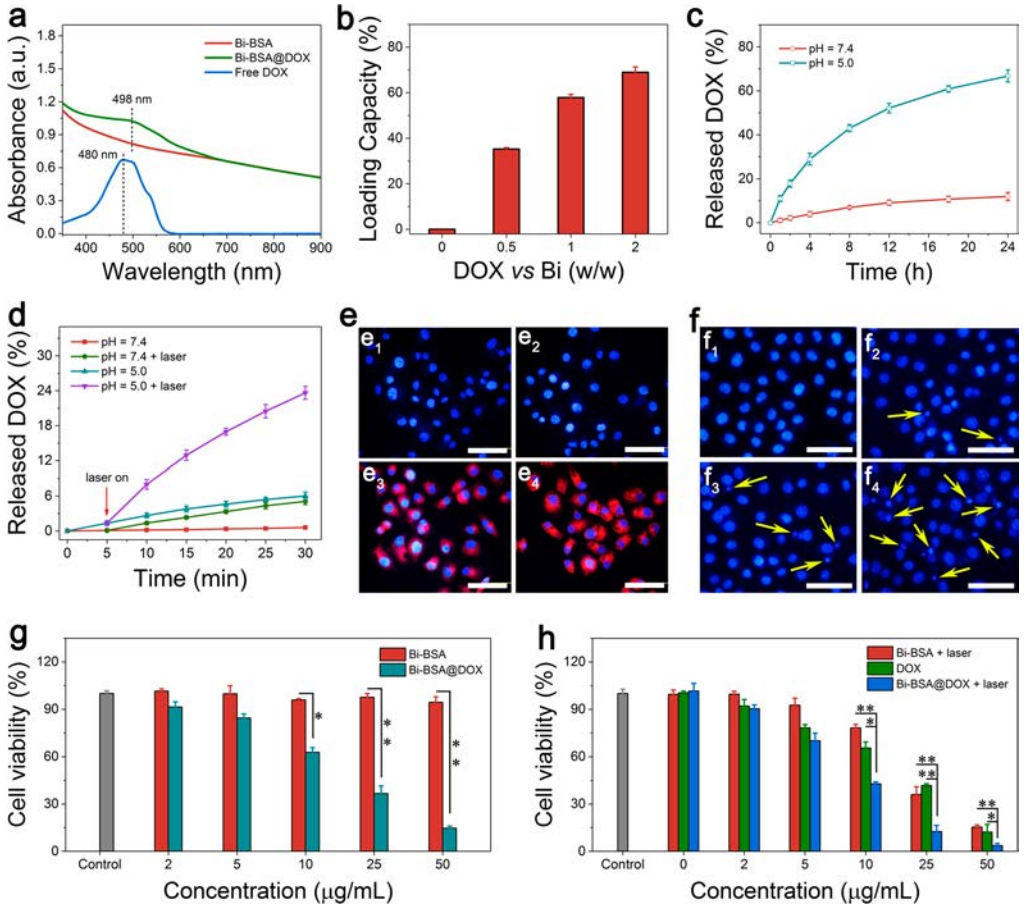


**Figure 4.** (a) UV−vis-NIR absorption spectra of free DOX, Bi-BSA and Bi-BSA@DOX. (b) DOX loading capacity versus the indicated mass ratio of the feeding DOX and Bi-BSA. (c) DOX release profiles at pH = 7.4 and 5.0 within 24 h. (d) DOX release profiles at pH = 7.4 and 5.0 with or without laser irradiation (1.0 W·cm$^{-2}$). (e) Fluorescence images of HeLa cells ($e_1$) before (the contol), or after treated with ($e_2$) the Bi-BSA, ($e_3$) the Bi-BSA@DOX, and ($e_4$) the Bi-BSA@DOX plus NIR laser, respectively. The blue and red signals represent the DAPI-stained cell nuclei and DOX fluorescence, respectively. Scale bar is 100 $\mu$m. (f) Cell nuclei morphology study of HeLa cells ($f_1$) before (the control), or after incubated with ($f_2$) 5 $\mu$g·mL$^{-1}$, ($f_3$) 10 $\mu$g·mL$^{-1}$, and ($f_4$) 15 $\mu$g·mL$^{-1}$ of the Bi-BSA@DOX dispersions for 24 h. Abnormal nuclear fragments are marked with the yellow arrows. Scale bar is 100 $\mu$m. (g) Cell viability of HeLa cells after treated with the Bi-BSA and Bi-BSA@DOX for 24 h. (h) Cell viability of HeLa cells after treated by the Bi-BSA plus NIR laser, free DOX, and the Bi-BSA@DOX plus NIR laser, respectively. Note that the free DOX concentration was equal to the loaded DOX in the Bi-BSA@DOX. Student's $t$ test, *$p$ < 0.05, **$p$ < 0.01.

results demonstrate the potentially excellent biocompatibility of the Bi-BSA NRs for biomedical applications.

Because Bi element has a higher X-ray attenuation coefficient than Au, Pt, Ta, and I,[29] the pure metallic Bi-BSA NRs with 100% Bi payload are anticipated to be a high-performance CT imaging agent. As shown in Figure 3a, brighter CT signals of the Bi-BSA NRs dispersions were observed at higher concentrations, revealing the incremental CT signal values. Importantly, the CT contrast enhanced efficiency was determined to be ∼66.7 HU·mL·mg$^{-1}$ ($R^2$ = 0.99). Such superhigh X-ray absorption coefficient is much higher than that of any other previously reported CT agents (such as I-based, Au-based, W-based, Ta-based, and bismuth chalcogenide-based CT agents).[27,33,53−58] We next carried out the in vivo CT imaging of the NRs using HeLa tumor-bearing mice. Only normal bone structures were seen before (Pre) the NRs injection (Figure 3b), while strong CT imaging signals in the tumor site were visualized immediately after (Post) injection (Figure 3c). These results suggest that the Bi-BSA NRs could serve as a highly effective CT imaging agent.

Besides CT imaging, the high NIR absorption and efficient photothermal conversion property endowed the Bi-BSA NRs great potentials for PA imaging, which is a noninvasive biomedical imaging modality with high imaging depth and spatial sensitivity/resolution.[59] As shown in Figure 3d,e, under NIR irradiation PA images with more pronounced signals were observed as the NRs concentrations increased gradually, and such PA signal enhancements increased monotonously with concentrations, suggesting the excellent PA imaging capacity. We then carried out the in vivo PA imaging of the NRs using HeLa tumor-bearing mice. As shown in Figure 3f,g, negligible PA signals were observable in the tumor site before injection, whereas PA signals in the tumor were remarkably enhanced after injection with ∼6.3-fold, ∼ 5.8-fold, and ∼4.2-fold enhancement of PA signal intensity when exposed to 700, 808, and 900 nm laser irradiation, respectively. The results reveal the great promises of the NRs as an efficient agent for PA imaging applicable to a wide range of NIR wavelengths.

Moreover, the Bi-BSA NRs can realize strong IRT imaging signals and significant temperature elevation on HeLa cells upon laser irradiation after incubation (Figure S21a,b). The results of live−dead cell staining assay (Figure S21c) show that the NRs could cause obvious cell death upon laser irradiation, and the photothermal killing efficacy remarkably enhanced



DOI: 10.1021/acs.nanolett.8b02639
Nano Lett. 2018, 18, 6778−6788

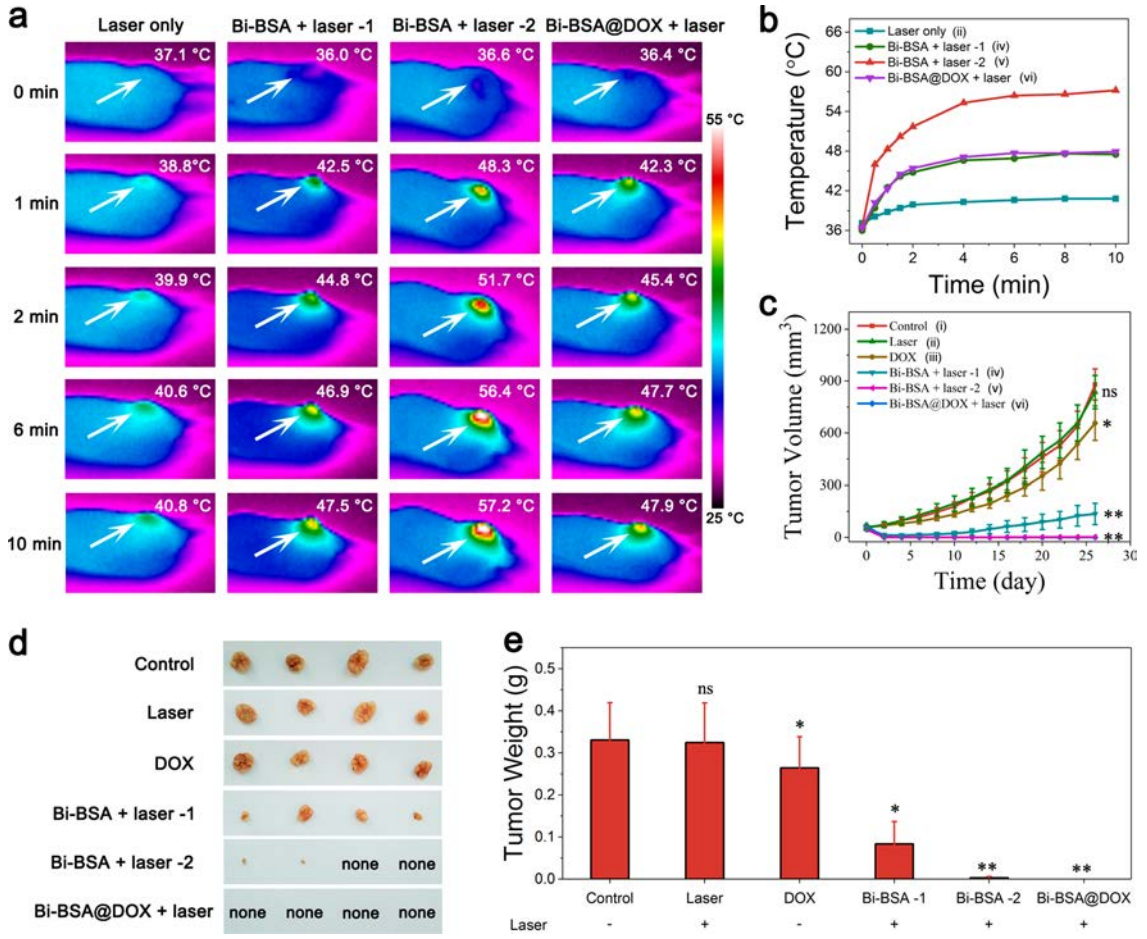


**Figure 5.** (a) In vivo IRT images of tumor-bearing mice treated with laser only, the Bi-BSA plus laser (the used dose of 2.0 mg·kg$^{-1}$ is denoted as Bi-BSA + laser −1, while the dose of 4.0 mg·kg$^{-1}$ is as Bi-BSA + laser −2), or the Bi-BSA@DOX (dose ∼2.0 mg·kg$^{-1}$) plus laser (Bi-BSA@DOX + laser). (b) Tumor-temperature variations in different groups. (c) Tumor growth profiles, (d) digital photos of tumors, and (e) the corresponding average tumor weights collected at the end of the experiment. Student's *t* test, ns: $p > 0.05$, *$p < 0.05$, **$p < 0.01$.

with an extended irradiation duration, or increased NRs concentration, or higher irradiation power density. Moreover, quantitative study via CCK-8 assay further revealed the strict irradiation duration-, concentration-, and power density-dependent manners of the photothermal killing efficacy (Figure S22a,b). All these results clearly demonstrate that the Bi-BSA NRs can act as a potent PTCA to mediate efficient photothermal destruction of cancer cells.

Because of the large SSA and highly porous nature, the Bi-BSA NRs hold a great potential to be loaded with antitumor drugs for chemotherapy. As a proof-of-concept study, we chose DOX (a broad-spectrum chemotherapeutic drug in clinic) as a model drug to evaluate their loading capacity. Compared with the absorption spectrum of the bare Bi-BSA NRs, the Bi-BSA@DOX NRs showed increased absorption in the range of 350−700 nm (Figure 4a), which is originated from the loaded DOX. The typical DOX absorption peak at ∼480 nm shifted to ∼498 nm in the spectrum of the Bi-BSA@DOX NRs, which is mainly due to the DOX hydrophobicity transformation and the strong interaction between DOX molecules and the NRs. Meanwhile, the successful DOX loading was also confirmed by zeta potential measurement (Figure S14), where the Bi-BSA@DOX showed less negative charge (−3.87 ± 0.91 mV) after loaded with positively charged DOX molecules. The NRs-DOX interaction can be attributed to the electrostatic/hydrophobic interaction between BSA and DOX together with the coordination between Bi metal and functional groups (−$NH_2$, −OH) in DOX molecules. In addition, the DOX loading capacity (DLC) increased commensurately with the amount of feeding DOX, and a DLC as high as ∼69% was obtained when the feeding DOX versus Bi (w/w) was 2:1 (Figure 4b). However, the DOX loading efficiency (DLE) gradually decreased as the feeding DOX/Bi mass ratios increased (Figure S23). Therefore, considering the economical utilization efficiency, we chose the feeding ratio of 1:1 (DOX vs Bi) for the following experiments.

The DOX releasing behavior was investigated in PBS solutions at different pH (5.0 and 7.4). The faintly acid pH (5.0) can induce faster DOX release rate than the neutral pH (7.4) (Figure 4c). The released DOX amount at pH 5.0 after 24 h reached ∼67%, much higher than that at pH = 7.4 (∼12%). The accelerated drug release is very likely due to the increased protonation and hydrophilia of DOX molecules under acid conditions. Moreover, a burst DOX release was observed upon laser irradiation (Figure 4d), indicating the laser-responsive drug release. This was mainly attributed to the rapid local temperature increase which could enhance thermal vibration to weaken the DOX-NRs interaction and accelerate DOX dissolution from the NRs.[33,34] In addition, such laser-responsive release was also potentiated in acidic environment. As a result, the released DOX amount at pH = 5.0 after 25 min irradiation was almost 4-fold as that without irradiation (24%



DOI: 10.1021/acs.nanolett.8b02639
Nano Lett. 2018, 18, 6778−6788

vs 6%). Since the tumor extracellular microenvironment and endosome/lysosome inside tumor cells are acid,[60,61] the Bi-BSA@DOX can therefore realize preferential drug release upon the targeted laser irradiation. Such bimodal pH- and NIR-responsive drug release capacity is preferred for on-demand drug delivery, minimizing the undesirable drug leakage and thus reducing side effects to normal tissues.

The intracellular drug delivery was studied by incubating HeLa cells with the Bi-BSA@DOX, followed by staining with 4′,6-diamidino-2-phenylindole (DAPI). As shown in Figure 4e and Figure S24, intense DOX fluorescence signals were observed in the cells incubated with the Bi-BSA@DOX ($e_3$), which was sharply different from the results of the control group ($e_1$) and Bi-BSA group ($e_2$). Moreover, the intracellular DOX fluorescence was obviously enhanced in the cells treated by the Bi-BSA@DOX plus irradiation ($e_4$), suggesting that NIR light can trigger more DOX release (consistent with results in Figure 4d). As the targeted active site of DOX mainly locates in the nucleus, we then studied the nuclear morphology of HeLa cells after treated with the Bi-BSA@DOX (Figure 4f and Figure S25). At variance with the control group ($f_1$), many abnormal nucleus fragments ($f_2$, $f_3$, $f_4$) were visible in HeLa cells treated by the Bi-BSA@DOX. The number of abnormal fragments were increased with the concentration, revealing the dose-dependent manner. CCK-8 assay was employed to measure the cell viability of HeLa cells after incubated with the Bi-BSA@DOX (Figure 4g). Consistently, a remarkable concentration-dependent decrease of the cell viability was observed for the cells after treated with the Bi-BSA@DOX, suggesting the efficient chemotherapy efficacy.

Next, the stimuli-responsive performance of the Bi-BSA@DOX for synergistic CPTT was explored. HeLa cells were treated by the Bi-BSA + laser (PTT), free DOX (chemotherapy), or the Bi-BSA@DOX + laser (CPTT) for cell viability measurement. As shown in Figure 4h, the CPTT group exhibited much stronger killing efficacy than either the PTT or chemotherapy group at all the tested concentrations. For instance, at 50 $\mu g \cdot mL^{-1}$, CPTT killed ~96.3% cancer cells, much higher than either PTT (~84.6%) or chemotherapy (~87.8%) alone. These results clearly demonstrate the superior synergetic antitumor effect of CPTT.

Given the fascinating in vitro results, we finally performed animal experiments to evaluate the in vivo antitumor efficacy. Before evaluation, we first conducted intravenous (i.v.) injection of the Bi-BSA NRs (injection dose ~40 $mg \cdot kg^{-1}$) to tumor-bearing mice to study if the NRs could passively accumulate into tumors. Twenty-four hours after i.v. injection, the mice were anesthetized and then irradiated by the laser. As shown in Figure S26, for the intravenously injected group the tumor temperature increased rapidly to ~46.2 °C and ~50.6 °C within 10 min irradiation at a laser power density of 1.0 and 1.5 $W \cdot cm^{-2}$, respectively, while the temperature of surrounding tissues adjacent to the tumor was barely elevated. These results reveal that the NRs can passively accumulated into the tumor sites via the enhanced permeability and retention (EPR) effect. In vivo biodistribution experiments (Figure S27) further confirm tumor accumulation of the NRs. Besides, a large amount of $Bi^{3+}$ was detected in the liver and spleen, suggesting the efficient uptake by the mononuclear phagocyte system.

To evaluate the in vivo antitumor efficacy, tumor-bearing mice were randomly divided into six groups ($n = 4$) as follows: (i) Control (no treatment), (ii) laser only, (iii) free DOX only, (iv) Bi-BSA + laser −1 (injection dose ~2.0 $mg \cdot kg^{-1}$), (v) Bi-BSA + laser −2 (injection dose ~4.0 $mg \cdot kg^{-1}$), and (vi) Bi-BSA@DOX + laser (injection dose ~2.0 $mg \cdot kg^{-1}$). The IRT images and tumor temperature changes of the groups (ii), (iv), (v), and (vi) upon laser irradiation (1.0 $W \cdot cm^{-2}$) were recorded by the IRT camera. As anticipated, both the Bi-BSA and Bi-BSA@DOX realized high-contrast IRT imaging on tumors (Figure 5a). The IRT imaging signals became more pronounced upon longer irradiation duration, revealing remarkable temperature elevation. After 10 min irradiation, the tumor temperature swiftly reached ~47.5 °C for group (iv), ~57.2 °C for group (v), and ~47.9 °C for group (vi), respectively (Figure 5b). Such high hyperthermia was sufficient to eliminate tumor cells. In contrast, for group (ii) treated with the irradiation alone, the tumor temperature was hardly changed (~3.7 °C) during the whole irradiation.

After irradiation, the tumors in groups (iv), (v), and (vi) were efficiently inhibited (Figure 5c and Figure S28), suggesting the prominent antitumor effect. Remarkably, group (v) with higher injection dose of the Bi-BSA showed stronger inhibition efficiency than group (iv), revealing the dose-dependent PTT efficacy. Importantly, all the tumors in CPTT group (vi) were completely eliminated and no regrowth was observed during the following 26-day observation. In marked contrast, negligible influence on the tumor growth was found in the control group (i) or laser only group (ii); while free DOX group (iii) only showed slight inhibition effect. At the end of therapy, the mice were sacrificed and the tumors were carefully stripped for weight measurements (Figure 5d and 5e). Consistent with in vitro results (Figure 4h), the CPTT can realize more efficient tumor regression than either chemotherapy or PTT (even a higher-dose PTT) alone. Furthermore, no obvious body weight loss (Figure S29), major organ weight loss (Figure S30), major organ injury (Figure S31) and abnormal blood parameters (Figure S32) were observed during the therapy. Therefore, our results suggest that the Bi-BSA NRs can serve as a promising theranostic nanosystem with high biocompatibility for cancer treatments.

In summary, we have successfully developed a highly porous Bi-BSA NRs platform for multimodal imaging, stimuli-responsive drug delivery, and synergistic chemo-photothermal combination therapy. Upon NIR irradiation, the NRs can efficiently absorb and convert light energy into heat for photothermal ablation of cancer cells. Chemotherapeutic DOX can be loaded into the NRs, exhibiting a controllable drug release manner sensitively triggered by the irradiation and acidic pH. Importantly, the CPTT therapeutic efficacy mediated by the NRs is superior to that of either monotherapy alone, as demonstrated both in vitro and in vivo. Preliminary toxicity studies reveal that such NRs have good biocompatibility without any appreciable toxicity to mice. Besides, benefiting from the strong photothermal conversion capacity and superhigh X-ray attenuation coefficient, the NRs are capable of serving as attractive multimodal contrast agents for high-performance IRT, PA, and CT triple-modal imaging. Such Bi-BSA NRs nanoplatform may pave a promising avenue for the development of more precise/efficient antitumor treatments.

## ■ ASSOCIATED CONTENT

### Supporting Information

The Supporting Information is available free of charge on the ACS Publications website at DOI: 10.1021/acs.nanolett.8b02639.



DOI: 10.1021/acs.nanolett.8b02639
Nano Lett. 2018, 18, 6778−6788

Materials and methods, figures showing additional characterizations (SEM, TEM, XRD, BET, and so forth), hemagglutination assay, DOX loading efficiency, intracellular drug delivery, in vivo IRT images, in vivo biodistribution, and in vivo toxicity assessment data (PDF)

## AUTHOR INFORMATION


### Corresponding Authors

*E-mail: miaoyu_che@hit.edu.cn. Phone: +86-451-86403708
*E-mail: peng.huang@szu.edu.cn. Phone: +86-755-86671911.
*E-mail: sunye@hit.edu.cn. Phone: +86-451-86414109.
*E-mail: fbe@inano.au.dk. Phone: +45-87156724.

### ORCID

Flemming Besenbacher: 0000-0003-0028-1335
Peng Huang: 0000-0003-3651-7813
Miao Yu: 0000-0001-8820-9594


### Notes

The authors declare no competing financial interest.

## ACKNOWLEDGMENTS

This work is financially supported by the National Natural Science Foundation of China (21473045, 51772066, 51573096, 31771036), the Fundamental Research Funds from the Central University (PIRS OF HIT A201503), Natural Science Foundation of Heilongjiang Province, China (E2015003), State Key Laboratory of Urban Water Resource and Environment, Harbin Institute of Technology (2018DX04), the Basic Research Program of Shenzhen (JCYJ20170412111100742, JCYJ20160422091238319), Guangdong Province Natural Science Foundation of Major Basic Research and Cultivation Project (2018B030308003), and the Fok Ying-Tong Education Foundation for Young Teachers in the Higher Education Institutions of China (161032).

## REFERENCES


(1) Chen, Y.; Chen, H.; Zeng, D.; Tian, Y.; Chen, F.; Feng, J.; Shi, J. Core/Shell Structured Hollow Mesoporous Nanocapsules: A Potential Platform for Simultaneous Cell Imaging and Anticancer Drug Delivery. *ACS Nano* **2010**, *4*, 6001−6013.

(2) Mackowiak, S. A.; Schmidt, A.; Weiss, V.; Argyo, C.; Von Schirnding, C.; Bein, T.; Bräuchle, C. Targeted Drug Delivery in Cancer Cells with Red-Light Photoactivated Mesoporous Silica Nanoparticles. *Nano Lett.* **2013**, *13*, 2576−2583.

(3) Zhu, C.; Huo, D.; Chen, Q.; Xue, J.; Shen, S.; Xia, Y. A Eutectic Mixture of Natural Fatty Acids Can. Serve as the Gating Material for Near-Infrared-Triggered Drug Release. *Adv. Mater.* **2017**, *29*, 1703702.

(4) Liu, J.; Bu, W.; Pan, L.; Shi, J. NIR-Triggered Anticancer Drug Delivery by Upconverting Nanoparticles with Integrated Azobenzene-Modified Mesoporous Silica. *Angew. Chem., Int. Ed.* **2013**, *52*, 4375−4379.

(5) Qian, C.; Yu, J.; Chen, Y.; Hu, Q.; Xiao, X.; Sun, W.; Wang, C.; Feng, P.; Shen, Q. D.; Gu, Z. Light-Activated Hypoxia-Responsive Nanocarriers for Enhanced Anticancer Therapy. *Adv. Mater.* **2016**, *28*, 3313−3320.

(6) Luo, Z.; Hu, Y.; Cai, K.; Ding, X.; Zhang, Q.; Li, M.; Ma, X.; Zhang, B.; Zeng, Y.; Li, P.; et al. Intracellular Redox-Activated Anticancer Drug Delivery by Functionalized Hollow Mesoporous Silica Nanoreservoirs with Tumor Specificity. *Biomaterials* **2014**, *35*, 7951−7962.

(7) Li, Z.; Hu, Y.; Jiang, T.; Howard, K. A.; Li, Y.; Fan, X.; Sun, Y.; Besenbacher, F.; Yu, M. Human-Serum-Albumin-Coated Prussian Blue Nanoparticles as pH-/Thermotriggered Drug-Delivery Vehicles for Cancer Thermochemotherapy. *Part. Part. Syst. Char.* **2016**, *33*, 53−62.

(8) Yang, P.; Gai, S.; Lin, J. Functionalized Mesoporous Silica Materials for Controlled Drug Delivery. *Chem. Soc. Rev.* **2012**, *41*, 3679−3698.

(9) Torchilin, V. P. Recent Advances with Liposomes as Pharmaceutical Carriers. *Nat. Rev. Drug Discovery* **2005**, *4*, 145−160.

(10) Jing, L.; Liang, X.; Li, X.; Yang, Y.; Dai, Z. Covalent Attachment of Mn-porphyrin onto Doxorubicin-Loaded Poly(Lactic Acid) Nanoparticles for Potential Magnetic Resonance Imaging and pH-Sensitive Drug Delivery. *Acta Biomater.* **2013**, *9*, 9434−9441.

(11) Xing, R.; Bhirde, A. A.; Wang, S.; Sun, X.; Liu, G.; Hou, Y.; Chen, X. Hollow Iron Oxide Nanoparticles as Multidrug Resistant Drug Delivery and Imaging Vehicles. *Nano Res.* **2013**, *6*, 1−9.

(12) Szakács, G.; Paterson, J. K.; Ludwig, J. A.; Boothgenthe, C.; Gottesman, M. M. Targeting Multidrug Resistance in Cancer. *Nat. Rev. Drug Discovery* **2006**, *5*, 219−234.

(13) Liu, H.; Chen, D.; Li, L.; Liu, T.; Tan, L.; Wu, X.; Tang, F. Multifunctional Gold Nanoshells on Silica Nanorattles: A Platform for the Combination of Photothermal Therapy and Chemotherapy with Low Systemic Toxicity. *Angew. Chem.* **2011**, *123*, 921−925.

(14) Chu, C.; Lin, H.; Liu, H.; Wang, X.; Wang, J.; Zhang, P.; Gao, H.; Huang, C.; Zeng, Y.; Tan, Y.; et al. Tumor Microenvironment-Triggered Supramolecular System as an In Situ Nanotheranostic Generator for Cancer Phototherapy. *Adv. Mater.* **2017**, *29*, 1605928.

(15) Yin, W.; Yan, L.; Yu, J.; Tian, G.; Zhou, L.; Zheng, X.; Zhang, X.; Yong, Y.; Li, J.; Gu, Z.; et al. High-Throughput Synthesis of Single-Layer $MoS_2$ Nanosheets as a Near-Infrared Photothermal-Triggered Drug Delivery for Effective Cancer Therapy. *ACS Nano* **2014**, *8*, 6922−6933.

(16) Akhter, S.; Ahmad, M. Z.; Ahmad, F. J.; Storm, G.; Kok, R. J. Gold Nanoparticles in Theranostic Oncology: Current State-of-the-art. *Expert Opin. Drug Delivery* **2012**, *9*, 1225−1243.

(17) Kong, F.; Zhang, H.; Qu, X.; Zhang, X.; Chen, D.; Ding, R.; Mäkilä, E.; Salonen, J.; Santos, H. A.; Hai, M. Gold Nanorods, DNA Origami, and Porous Silicon Nanoparticle-functionalized Biocompatible Double Emulsion for Versatile Targeted Therapeutics and Antibody Combination Therapy. *Adv. Mater.* **2016**, *28*, 10195−10203.

(18) Li, Z.; Zeng, Y.; Zhang, D.; Wu, M.; Wu, L.; Huang, A.; Yang, H.; Liu, X.; Liu, J. Glypican-3 Antibody Functionalized Prussian Blue Nanoparticles for Targeted MR Imaging and Photothermal Therapy of Hepatocellular Carcinoma. *J. Mater. Chem. B* **2014**, *2*, 3686−3696.

(19) Shah, J.; Park, S.; Aglyamov, S.; Larson, T.; Ma, L.; Sokolov, K.; Johnston, K.; Milner, T.; Emelianov, S. Y. Photoacoustic Imaging and Temperature Measurement for Photothermal Cancer Therapy. *J. Biomed. Opt.* **2008**, *13*, 034024.

(20) Kangasniemi, M.; Mcnichols, R. J.; Bankson, J. A.; Gowda, A.; Price, R. E.; Hazle, J. D. Thermal Therapy of Canine Cerebral Tumors Using a 980 nm Diode Laser with MR Temperature-Sensitive Imaging Feedback. *Lasers Surg. Med.* **2004**, *35*, 41−50.

(21) Wu, Y. L.; Engl, W.; Hu, B.; Cai, P.; Leow, W. R.; Tan, N. S.; Lim, C. T.; Chen, X. Nanomechanically Visualizing Drug-Cell Interaction at the Early Stage of Chemotherapy. *ACS Nano* **2017**, *11*, 6996−7005.

(22) Cai, P.; Layani, M.; Leow, W. R.; Amini, S.; Liu, Z.; Qi, D.; Hu, B.; Wu, Y. L.; Miserez, A.; Magdassi, S.; et al. Bio-Inspired Mechanotactic Hybrids for Orchestrating Traction-Mediated Epithelial Migration. *Adv. Mater.* **2016**, *28*, 3102−3110.

(23) Hu, B.; Leow, W. R.; Amini, S.; Nai, B.; Zhang, X.; Liu, Z.; Cai, P.; Li, Z.; Wu, Y. L.; Miserez, A.; et al. Orientational Coupling Locally Orchestrates a Cell Migration Pattern for Re-Epithelialization. *Adv. Mater.* **2017**, *29*, 1700145.

(24) Hu, B.; Leow, W. R.; Cai, P.; Li, Y. Q.; Wu, Y. L.; Chen, X. Nanomechanical Force Mapping of Restricted Cell-To-Cell Collisions Oscillating between Contraction and Relaxation. *ACS Nano* **2017**, *11*, 12302−12310.




DOI: 10.1021/acs.nanolett.8b02639
*Nano Lett.* 2018, 18, 6778−6788

(25) Zhang, Z.; Wang, L.; Wang, J.; Jiang, X.; Li, X.; Hu, Z.; Ji, Y.; Wu, X.; Chen, C. Mesoporous Silica-Coated Gold Nanorods as a Light-Mediated Multifunctional Theranostic Platform for Cancer Treatment. *Adv. Mater.* **2012**, *24*, 1418−1423.
(26) Li, W.; Rong, P.; Yang, K.; Huang, P.; Sun, K.; Chen, X. Semimetal Nanomaterials of Antimony as Highly Efficient Agent for Photoacoustic Imaging and Photothermal Therapy. *Biomaterials* **2015**, *45*, 18−26.
(27) Cheng, L.; Liu, J.; Gu, X.; Gong, H.; Shi, X.; Liu, T.; Wang, C.; Wang, X.; Liu, G.; Xing, H.; et al. PEGylated $WS_2$ Nanosheets as A Multifunctional Theranostic Agent for *In Vivo* Dual-Modal CT/Photoacoustic Imaging Guided Photothermal Therapy. *Adv. Mater.* **2014**, *26*, 1886−1893.
(28) Zha, Z.; Yue, X.; Ren, Q.; Dai, Z. Uniform Polypyrrole Nanoparticles with High Photothermal Conversion Efficiency for Photothermal Ablation of Cancer Cells. *Adv. Mater.* **2013**, *25*, 777−782.
(29) Li, J.; Jiang, F.; Yang, B.; Song, X. R.; Liu, Y.; Yang, H. H.; Cao, D. R.; Chen, G. N.; et al. Topological Insulator Bismuth Selenide as A Theranostic Platform for Simultaneous Cancer Imaging and Therapy. *Sci. Rep.* **2013**, *3*, 1998.
(30) Zhang, X.; Chen, J.; Min, Y.; Park, G. B.; Shen, X.; Song, S.; Sun, Y.; Wang, H.; Long, W.; Xie, J.; et al. Metabolizable $Bi_2Se_3$ Nanoplates: Biodistribution, Toxicity, and Uses for Cancer Radiation Therapy and Imaging. *Adv. Funct. Mater.* **2014**, *24*, 1718−1729.
(31) Mao, F.; Wen, L.; Sun, C.; Zhang, S.; Wang, G.; Zeng, J.; Wang, Y.; Ma, J.; Gao, M.; Li, Z. Ultrasmall Biocompatible $Bi_2Se_3$ Nanodots for Multimodal Imaging-Guided Synergistic Radiophotothermal Therapy against Cancer. *ACS Nano* **2016**, *10*, 11145−11155.
(32) Wang, Y.; Wu, Y.; Liu, Y.; Shen, J.; Lv, L.; Li, L.; Yang, L.; Zeng, J.; Wang, Y.; Zhang, L. W.; et al. BSA-Mediated Synthesis of Bismuth Sulfide Nanotheranostic Agents for Tumor Multimodal Imaging and Thermoradiotherapy. *Adv. Funct. Mater.* **2016**, *26*, 5335−5344.
(33) Li, Z.; Liu, J.; Hu, Y.; Howard, K. A.; Li, Z.; Fan, X.; Chang, M.; Sun, Y.; Besenbacher, F.; Chen, C.; et al. Multimodal Imaging-Guided Antitumor Photothermal Therapy and Drug Delivery Using Bismuth Selenide Spherical-Sponge. *ACS Nano* **2016**, *10*, 9646−9658.
(34) Li, Z.; Hu, Y.; Chang, M.; Howard, K. A.; Fan, X.; Sun, Y.; Besenbacher, F.; Yu, M. Highly porous PEGylated $Bi_2S_3$ Nano-Urchins as A Versatile Platform for *In Vivo* Triple-Modal Imaging, Photothermal Therapy and Drug Delivery. *Nanoscale* **2016**, *8*, 16005−16016.
(35) Li, Z.; Hu, Y.; Howard, K. A.; Jiang, T.; Fan, X.; Miao, Z.; Sun, Y.; Besenbacher, F.; Yu, M. Multifunctional Bismuth Selenide Nanocomposites for Antitumor Thermo-Chemotherapy and Imaging. *ACS Nano* **2016**, *10*, 984−997.
(36) Li, Z.; Liu, J.; Hu, Y.; Li, Z.; Fan, X.; Sun, Y.; Besenbacher, F.; Chen, C.; Yu, M. Biocompatible PEGylated Bismuth Nanocrystals: "All-In-One" Theranostic Agent with Triple-Modal Imaging and Efficient *In Vivo* Photothermal Ablation of Tumors. *Biomaterials* **2017**, *141*, 284−295.
(37) Lei, P.; An, R.; Zhang, P.; Yao, S.; Song, S.; Dong, L.; Xu, X.; Du, K.; Feng, J.; Zhang, H. Ultrafast Synthesis of Ultrasmall Poly(Vinylpyrrolidone)-Protected Bismuth Nanodots as a Multifunctional Theranostic Agent for *In Vivo* Dual-Modal CT/Photothermal-Imaging-Guided Photothermal Therapy. *Adv. Funct. Mater.* **2017**, *27*, 1702018.
(38) Yu, X.; Li, A.; Zhao, C.; Yang, K.; Chen, X.; Li, W. Ultrasmall Semimetal Nanoparticles of Bismuth for Dual-Modal Computed Tomography/Photoacoustic Imaging and Synergistic Thermoradiotherapy. *ACS Nano* **2017**, *11*, 3990−4001.
(39) Bao, T.; Yin, W.; Zheng, X.; Zhang, X.; Yu, J.; Dong, X.; Yong, Y.; Gao, F.; Yan, L.; Gu, Z.; et al. One-Pot Synthesis of PEGylated Plasmonic $MoO_{3-x}$ Hollow Nanospheres for Photoacoustic Imaging Guided Chemo-Photothermal Combinational Therapy of Cancer. *Biomaterials* **2016**, *76*, 11−24.
(40) Ma, M.; Huang, Y.; Chen, H.; Jia, X.; Wang, S.; Wang, Z.; Shi, J. $Bi_2S_3$-Embedded Mesoporous Silica Nanoparticles for Efficient Drug Delivery and Interstitial Radiotherapy Sensitization. *Biomaterials* **2015**, *37*, 447−455.
(41) Li, Z.; Li, Z.; Sun, L.; Du, B.; Wang, Y.; Zhao, G.; Yu, D.; Yang, S.; Sun, Y.; Yu, M. Core-Shell $Bi_2Se_3$@$mSiO_2$-PEG as a Multifunctional Drug-Delivery Nanoplatform for Synergistic Thermo-Chemotherapy with Infrared Thermal Imaging of Cancer Cells. *Part. Part. Syst. Char.* **2018**, *35*, 1700337.
(42) Guo, Z.; Zhu, S.; Yong, Y.; Zhang, X.; Dong, X.; Du, J.; Xie, J.; Wang, Q.; Gu, Z.; Zhao, Y. Synthesis of BSA-Coated BiOI@$Bi_2S_3$ Semiconductor Heterojunction Nanoparticles and Their Applications for Radio/Photodynamic/Photothermal Synergistic Therapy of Tumor. *Adv. Mater.* **2017**, *29*, 1704136.
(43) Yong, Y.; Zhou, L.; Zhang, S.; Yan, L.; Gu, Z.; Zhang, G.; Zhao, Y. Gadolinium Polytungstate Nanoclusters: a New Theranostic with Ultrasmall Size and Versatile Properties for Dual-Modal MR/CT Imaging and Photothermal Therapy/Radiotherapy of Cancer. *NPG Asia Mater.* **2016**, *8*, e273.
(44) Wang, Y.; Yang, T.; Ke, H.; Zhu, A.; Wang, J.; Shen, J.; Liu, G.; Chen, C.; Zhao, Y.; et al. Smart Albumin-Biomineralized Nanocomposites for Multimodal Imaging and Photothermal Tumor Ablation. *Adv. Mater.* **2015**, *27*, 3874−3882.
(45) Xie, J.; Zheng, Y.; Ying, J. Y. Protein-Directed Synthesis of Highly Fluorescent Gold Nanoclusters. *J. Am. Chem. Soc.* **2009**, *131*, 888−889.
(46) Wang, Y.; Wu, Y.; Liu, Y.; Shen, J.; Lv, L.; Li, L.; Yang, L.; Zeng, J.; Wang, Y.; Zhang, L. W.; et al. BSA-Mediated Synthesis of Bismuth Sulfide Nanotheranostic Agents for Tumor Multimodal Imaging and Thermoradiotherapy. *Adv. Funct. Mater.* **2016**, *26*, 5335−5344.
(47) Wang, Y.; Lang, L.; Huang, P.; Wang, Z.; Jacobson, O.; Kiesewetter, D. O.; Ali, I. U.; Teng, G.; Niu, G.; Chen, X. *In Vivo* Albumin Labeling and Lymphatic Imaging. *Proc. Natl. Acad. Sci. U. S. A.* **2015**, *112*, 208−213.
(48) Weissleder, R. A Clearer Vision for *In Vivo* Imaging. *Nat. Biotechnol.* **2001**, *19*, 316−317.
(49) Hessel, C. M.; Pattani, V. P.; Rasch, M.; Panthani, M. G.; Koo, B.; Tunnell, J. W.; Korgel, B. A. Copper Selenide Nanocrystals for Photothermal Therapy. *Nano Lett.* **2011**, *11*, 2560−2566.
(50) Roper, D. K.; Ahn, W.; Hoepfner, M. Microscale Heat Transfer Transduced by Surface Plasmon Resonant Gold Nanoparticles. *J. Phys. Chem. C* **2007**, *111*, 3636−3641.
(51) Sun, X.; Du, R.; Li, Z.; Zhang, G.; Zheng, X.; Qian, J.; Tian, X.; Zhou, J.; He, J.; Wang, Y.; et al. A pH-Responsive Yolk-Like Nanoplatform for Tumor Targeted Dual-Mode Magnetic Resonance Imaging and Chemotherapy. *ACS Nano* **2017**, *11*, 7049−7059.
(52) Yun, Y. S.; Teng, Z.; Hui, Y.; Shou, J. W.; Ying, T.; Yun, L. Z.; Wen, F. L.; Wei, T.; Li, J. Z.; Nan, L. A Multifunctional PB@$mSiO_2$-PEG/DOX Nanoplatform for Combined Photothermal-Chemotherapy of Tumor. *ACS Appl. Mater. Interfaces* **2016**, *8*, 17038−17046.
(53) Liu, J.; Zheng, X.; Yan, L.; Zhou, L.; Tian, G.; Yin, W.; Wang, L.; Liu, Y.; Hu, Z.; Gu, Z.; et al. Bismuth Sulfide Nanorods as A Precision Nanomedicine for *In Vivo* Multimodal Imaging-Guided Photothermal Therapy of Tumor. *ACS Nano* **2015**, *9*, 696−707.
(54) Kim, D.; Park, S.; Lee, J. H.; Yong, Y. J.; Jon, S. Antibiofouling Polymer-Coated Gold Nanoparticles as A Contrast Agent for *In Vivo* X-Ray Computed Tomography Imaging. *J. Am. Chem. Soc.* **2007**, *129*, 7661−7665.
(55) Ke, H.; Yue, X.; Wang, J.; Xing, S.; Zhang, Q.; Dai, Z.; Tian, J.; Wang, S.; Jin, Y. Gold Nanoshelled Liquid Perfluorocarbon Nanocapsules for Combined Dual Modal Ultrasound/CT Imaging and Photothermal Therapy of Cancer. *Small* **2014**, *10*, 1220−1227.
(56) Cheng, L.; Yuan, C.; Shen, S.; Yi, X.; Gong, H.; Yang, K.; Liu, Z. Bottom-Up Synthesis of Metal-Ion-Doped $WS_2$ Nanoflakes for Cancer Theranostics. *ACS Nano* **2015**, *9*, 11090−11101.
(57) Oh, M. H.; Lee, N.; Kim, H.; Park, S. P.; Piao, Y.; Lee, J.; Jun, S. W.; Moon, W. K.; Choi, S. H.; Hyeon, T. Large-Scale Synthesis of Bioinert Tantalum Oxide Nanoparticles for X-ray Computed Tomography Imaging and Bimodal Image-Guided Sentinel Lymph Node Mapping. *J. Am. Chem. Soc.* **2011**, *133*, 5508−5515.


DOI: 10.1021/acs.nanolett.8b02639
*Nano Lett.* 2018, 18, 6778−6788

(58) Jin, Y.; Li, Y.; Ma, X.; Zha, Z.; Shi, L.; Tian, J.; Dai, Z. Encapsulating Tantalum Oxide into Polypyrrole Nanoparticles for X-ray CT/Photoacoustic Bimodal Imaging-Guided Photothermal Ablation of Cancer. *Biomaterials* **2014**, *35*, 5795−5804.
(59) Ku, G.; Zhou, M.; Song, S.; Huang, Q.; Hazle, J.; Li, C. Copper Sulfide Nanoparticles as a New Class of Photoacoustic Contrast Agent for Deep Tissue Imaging at 1064 nm. *ACS Nano* **2012**, *6*, 7489−7496.
(60) Chen, X.; Chen, Z.; Hu, B.; Cai, P.; Wang, S.; Xiao, S.; Wu, Y. L.; et al. Synergistic Lysosomal Activatable Polymeric Nanoprobe Encapsulating pH Sensitive Imidazole Derivative for Tumor Diagnosis. *Small* **2018**, *14*, 1703164.
(61) Cai, P.; Leow, W. R.; Wang, X.; Wu, Y. L.; Chen, X. Programmable Nano-Bio Interfaces for Functional Biointegrated Devices. *Adv. Mater.* **2017**, *29*, 1605529.



DOI: 10.1021/acs.nanolett.8b02639
*Nano Lett.* 2018, 18, 6778−6788